

Protostellar cores in Sagittarius B2

NAZAR BUDAIEV ,¹ ADAM GINSBURG ,¹ DESMOND JEFF ,¹ CIRIACO GODDI ,^{2, 3, 4, 5}
FANYI MENG ,^{6, 7} ÁLVARO SÁNCHEZ-MONGE ,^{8, 9} PETER SCHILKE,⁷ ANIKA SCHMIEDEKE,¹⁰ AND
TAEHWAN YOO¹

¹ Department of Astronomy, University of Florida, P.O. Box 112055, Gainesville, FL 32611-2055, USA

² Universidade de São Paulo, Instituto de Astronomia, Geofísica e Ciências Atmosféricas, Departamento de Astronomia, São Paulo, SP 05508-090, Brazil

³ Dipartimento di Fisica, Università degli Studi di Cagliari, SP Monserrato-Sestu km 0.7, I-09042 Monserrato, Italy

⁴ INAF - Osservatorio Astronomico di Cagliari, via della Scienza 5, I-09047 Selargius (CA), Italy

⁵ INFN, Sezione di Cagliari, Cittadella Univ., I-09042 Monserrato (CA), Italy

⁶ University of Chinese Academy of Sciences, Beijing 100049, PR China

⁷ Physikalisch Institut der Universität zu Köln, Zülpicher Str. 77, 50937 Köln, Germany

⁸ Institut de Ciències de l'Espai (ICE, CSIC), Can Magrans s/n, E-08193, Bellaterra, Barcelona, Spain

⁹ Institut d'Estudis Espacials de Catalunya (IEEC), Barcelona, Spain

¹⁰ Green Bank Observatory, PO Box 2, Green Bank, WV 24944, USA

ABSTRACT

We present 500 AU and 700 AU resolution 1 mm and 3 mm ALMA observations, respectively, of protostellar cores in the giant molecular cloud Sagittarius B2 (Sgr B2), the most active star forming cloud in our Galaxy. Previous lower resolution (5000 AU) 3 mm observations of this region detected 110 sources inferred to be young stellar objects (YSOs) with $M > 8 M_{\odot}$. With a tenfold increase in resolution, we detect 371 sources at 3 mm and 222 sources in the smaller field of view at 1 mm. The sources seen at low resolution are observed to fragment into an average of two objects. About a third of the observed sources fragment. Most of the sources we report are marginally resolved and are at least partially optically thick. We determine that the observed sources are most consistent with Stage 0/I YSOs, i.e., rotationally supported disks with an active protostar and an envelope, that are warmer than those observed in the solar neighborhood. We report source-counting-based inferred stellar mass and the star formation rate of the cloud: $2300 M_{\odot}$, $0.0031 M_{\odot} \text{ yr}^{-1}$ for Sgr B2 N and $6300 M_{\odot}$, $0.0085 M_{\odot} \text{ yr}^{-1}$ for Sgr B2 M.

1. INTRODUCTION

Many stars in our Galaxy were formed around cosmic noon ($z \sim 2$, Madau & Dickinson 2014) under conditions rarely seen today. To study

the conditions under which an average Galactic star formed, we need to identify cosmic noon analogue star-forming regions. One such local environment analogue is present in the high-density, turbulent and overall extreme Central Molecular Zone (CMZ) (Henshaw et al. 2016). This is the only environment with such condi-

Corresponding author: Nazar Budaiev
nbudaiev@ufl.edu

tions where we can resolve disk scales (~ 100 s AU).

In young star clusters such as the Arches and Quintuplet, there is evidence of a top-heavy IMF (Hosek et al. 2019; Gallego-Calvente et al. 2022). Peering into early stages of star formation in the CMZ can help us understand if the IMF varies systematically with local environmental conditions and thus is shallower in the early universe.

The densest star forming cloud in our galaxy, Sagittarius B2 (Sgr B2), is a powerful laboratory for studying star formation and evolution in the highest-density region where we can resolve disk scales.

The Galactic center located at a distance of 8.127 ± 0.031 kpc (GRAVITY Collaboration et al. 2018) and Sgr B2 is ~ 100 pc away from the Galactic center in projection. Throughout this paper we assume a distance to Sgr B2 of 8.4 kpc to stay consistent with the similar work by Ginsburg et al. (2018). The molecular cloud is split into several smaller, concentrated regions of star formation: North (N), Main (M), South (S), and Deep South (DS). A large fraction ($\sim 25\text{--}50\%$) of the current star formation in this cloud occurs in the N and M regions, with many stars forming in bound clusters (Ginsburg et al. 2018; Schmiedeke et al. 2016). Half of the total star formation in the CMZ occurs in Sgr B2, despite containing $\sim 10\%$ of the mass ($8 \times 10^6 M_\odot$) and $< 1\%$ of the volume (5×10^4 pc 3 ; Ginsburg et al. 2018; Barnes et al. 2017; Schmiedeke et al. 2016).

Sgr B2 appears to be forming stars preferentially in dense, bound clusters (Ginsburg et al. 2018; Ginsburg & Kruijssen 2018). Since other Galactic Center star clusters have excesses of high-mass stars (Hosek et al. 2019; Gallego-Calvente et al. 2022), Sgr B2 is likely also forming extra massive stars. 3500 AU resolution observations towards Sgr B2 N and M suggest the presence of an excess of massive stars in the re-

gion (Sánchez-Monge et al. 2017). If this excess is present, it indicates a systematic variation of the stellar IMF with gas conditions, with a shallower IMF under conditions prevalent in galaxies with rapid star formation.

We report follow-up ALMA observations to ALMA project 2013.1.00269.S, which covered a 15×15 pc area around the Sgr B2 complex at 3 mm (Ginsburg et al. 2018) with ~ 5000 AU resolution. Our data covers Sgr B2 N and M at 3 mm and at 1 mm. We establish the possible nature and evolutionary stage of the sources. We place lower limits on cores' masses in the attempt to understand whether the IMF is top-heavy in young cluster and varies with the surrounding conditions.

In Section 2 we describe the observations and the imaging and self-calibration procedures. We then explain the source extraction approach in Section 3, make a comparison with previous low-resolution observations, and explain the way the spectral index was calculated between 3 mm and 1 mm. In Section 4 we show that our sources are consistent with Stage 0/I YSOs by ruling out other possible options. We also present calculations of the inferred stellar mass of the cloud and the star formation rate and present the multiplicity function. The paper is summarized in Section 5. In the appendices we briefly discuss the details of cleaning and self-calibration testing, radial core distribution for each protocluster, and show the fragmentation dependence on flux.

2. OBSERVATIONS AND DATA REDUCTION

This paper utilizes the data from ALMA Cycle 4 project 2016.1.00550.S. The observations consist of two pointings centered on Sgr B2 N (ICRS 17:47:19.925 -028.22.18.608) and Sgr B2 M (ICRS 17:47:20.174 -28.23.04.788) with the 12m antennas. Both locations were observed in Band 3 and Band 6 with resolution of $0.096'' \times 0.073''$ (~ 700 AU) and $0.083'' \times 0.038''$ (~ 500

AU), respectively. The pointings cover 6.5×4.5 pc at 3 mm and roughly 1.75×3.75 pc at 1 mm out to primary beam level of 0.1. The spectral setup for each Band consists of 4 spectral windows with 1920 channels each and channel frequency width of 976.6 kHz (1.875 GHz bandwidth), which corresponds to spectral resolution of ~ 1.3 km/s at 226 GHz and ~ 3.2 km/s at 92 GHz. The central spectral window frequencies are 217.84, 219.79, 231.80, and 233.67 GHz for Band 6 and 85.47, 87.37, 97.42, and 99.42 GHz for Band 3.

The data were imaged using CASA version 5.7.0-134.el7 `tclean` with robust parameter set to 0.5 (McMullin et al. 2007). No line subtraction or flagging was performed. Despite in the overlap between the Band 3 pointings, we used the standard gridded instead of the mosaic gridded. The initial cleaned images contained many imaging artifacts, such as radial streaks, circular patterns, and parallel “wavy” streaks. Therefore, we decided to self-calibrate the data to improve the quality of the final image. A detailed explanation of the tested approaches is presented in Appendix A. In summary, our standard self-calibration procedure consisted of the following steps:

1. Use one of the fully calibrated images from prior testing to estimate the lowest noise in the image. We measured the RMS in a box around an emission-free region close to the center of the image.
2. Use the same previously cleaned image to create a “strict” contour mask at six- σ threshold.
3. Using the same image, draw a “broad” mask that covers all regions where signal is present, even if it includes some artifacts or noise.
4. Clean the image with the `tclean` threshold parameter set to six times the noise

from step 1, and using the “strict” mask from step 2.

5. Complete a phase self-calibration with `solint` set to `inf`.
6. Repeat the clean from step 4.
7. Self-calibrate the image with `solint` set to `int`.
8. Clean the image with the `tclean` threshold parameter set to three times the noise from step 1 and using the “broad” mask from step 3.
9. Complete a round of phase and amplitude self-calibration with `solint` set to `inf`.
10. Repeat the clean from step 9.

However, some of the fields required further tuning to achieve better results. The Sgr B2 N Band 6 pointing suffered from divergence at the selected threshold values. Thus, we opted to increase the cleaning threshold up to ten times the noise until the amplitude self-calibration step was completed. After, we cleaned to three times the noise and added an extra amplitude and phase self-calibration step, which improved the image significantly. The Sgr B2 N Band 3 pointing did not benefit from the amplitude self-calibration step and introduced additional minor artifacts. Thus, we used the pre-amplitude-self-calibration image for our analysis. The final images for each Band are shown in Figures 1 and 2.

The final average RMS in an emission-free region close to the center the image for each of the pointings is 0.033 mJy for N Band 3, 0.05 mJy for M Band 3, 0.35 mJy for N Band 6, and 0.25 mJy for M Band 6.

3. ANALYSIS

3.1. Source extraction

We strove to make the catalog as reproducible as possible, while minimizing the number of

Table 1. Summary of the observations

Central frequency GHz	Date	$t_{science}$ seconds	Baseline length range meters	# of antennas
92.45	18-Sep-2017	2642	41-12100	43
92.45	18-Sep-2017	2644	41-12100	43
225.76	07-Sep-2017	2977	41-7600	46
225.76	16-Sep-2017	2973	41-12100	46

false positives. Automating source extraction presents numerous problems in a region like Sgr B2. The images have high dynamic range (~ 5000), contain complex extended structures, and like all interferometric single-pointing data, have radially varying noise. Combining this with the irregular structure of the observed objects makes fully automated source detection inefficient. Therefore, we utilized the automated source-finding dendrogram algorithm (Rosolowsky et al. 2008) augmented with a by-hand approach described below.

To avoid double counting sources we crop the overlapping parts of Band 3 imaged. The cut was made close to equidistant from the centers of the pointing, while not breaking up any regions with signal – just south of (below) H II region Sgr B2 Z10.24. We divide each primary-beam corrected image in 30 concentric annuli and a circle at the center. We then use 7-sigma clipping to remove most of the signal from each of the annuli and calculate the standard deviation for each region. This noise measurement is then used as `astrodendro` input parameters.

The central part of the pointings are signal-dominated, which, even after sigma clipping, results in a higher measured noise. The calculated noise as a function of radius rapidly drops beyond the central clusters and then gradually increases due to primary beam attenuation. We replace the estimated noise of the central part of the pointing with the lowest calculated value in the whole image such that the noise never decreases with radius.

Then, we perform source detection on the primary-beam-corrected images using the `astrodendro` source-finding algorithm. We generate a separate dendrogram for each concentric ring using noise estimation for input parameters. We run the dendrogram on the full image and then exclude any sources with centers outside of the ring. We set *min_value* to be equal to four times the noise estimate, *min_delta* to be 0.7 times the estimated noise, and *min_npix* to be 3 pixels.¹ The final source extraction thresholds are ~ 0.15 mJy at 3 mm and 1.2 mJy at 1 mm within the inner 40% of the observed area, and ~ 0.5 mJy at 3 mm and 4 mJy at 1 mm within the inner 90% of the observed area.

We then closely examine by eye parts of the image that contain extended structure and no compact emission, primarily H II regions. We draw polygons² around these locations by hand so that any detections within them can be excluded. In a few cases, we found core-like sources within the H II regions. We drew the polygons in a way that would include such sources in the final catalog.

¹ We tested a variety of combination of number of concentric rings (10, 15, 20, 30), *min_value* (3σ , 4σ , 5σ), *min_delta* (0.5, 0.7, 1.0), and *min_npix* (2, 3, 5). We inspected each combination by hand to find a compromise between reducing the number of false positives due to artifacts and noise and increasing the number of likely positives.

² The polygon regions are available on GitHub with the rest of the reduction code: https://github.com/bazarsen/SgrB2_ALMA_continuum

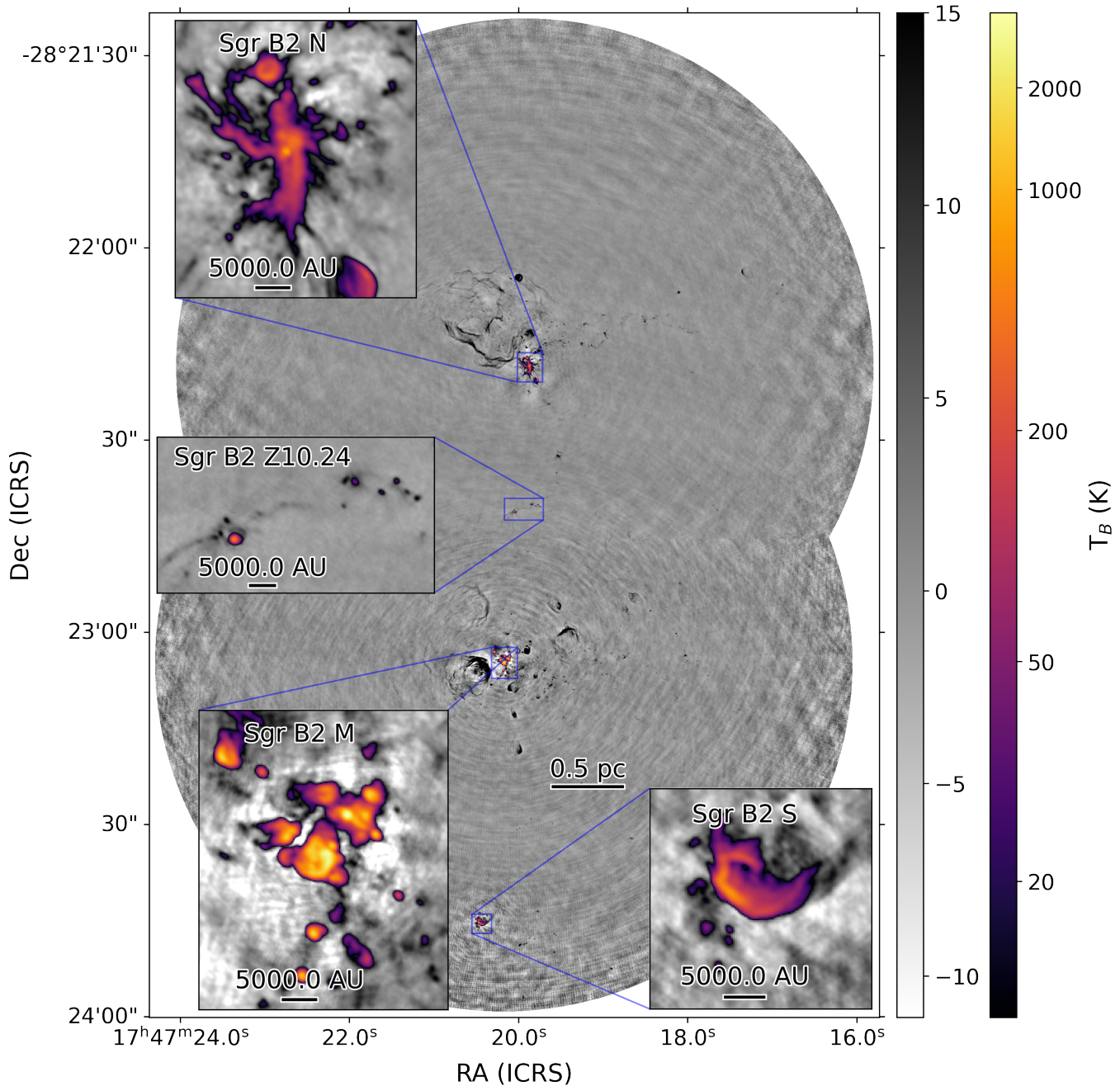


Figure 1. Band 3 (3 mm) continuum image of Sagittarius B2 N and M. The two pointings were imaged separately and then the final images were cut and overlaid to not overlap. The images were subsequently stitched together; the pixels in the central zoom-in come from only the N pointing. The insets show the high-density regions of Sgr B2 N and M, as well as Sgr B2 S and a region around H II region Sgr B2 Z10.24.

Finally, we review each of the catalogued sources in both pointings and frequencies by hand. We rank every source as not-a-core (0), core candidate (1), or core (2). We inspect each source twice: first, zoomed-in closely to examine the shape and the background features and then using the whole image to get context on the source morphology based on location and proximity to other sources.

For example, if a source with a score of 1 that resembles a filamentary structure is located close to an area with extended emission, such as an HII region, we mark it as a false detection and adjust the score accordingly. If such a source is located in a cluster of other sources with a score of 2 and is not visibly a part of any extended structure, we change its score to 2. We further investigate each source with a score of 1 by comparing their structure in the 1 mm and 3 mm data. If a potential source is part of a filamentary structure at 3 mm, but no local peak is observed at 1 mm, we score such a source as a 0. Such a filamentary structure at 3 mm without a strong counterpart at 1 mm is indicative of free-free emission.

All of the extended HII regions are excluded manually using polygons as described above. In addition, we cross-match our detections with De Pree et al. (1998) and Meng et al. (2022) to remove known compact HII regions from our core sample and label them as known HII regions. We find that VLA-detected HII regions do not perfectly align with HII region candidates in our data, especially in Sgr B2 M. We attribute this to poor absolute pointing accuracy of the VLA (Mills et al. 2018). When it is not possible to establish a confident one-to-one match between catalogs we label the source as an HII region candidate. Some of the previously known HII regions appear to have multiple peaks within their areas. We label these “fragmented” sources as HII region candidates.

To further indentify HII regions based on their spectral properties, we create a 1 mm to 3 mm spectral index map of the central, most dense parts of Sgr B2 N and M. We find that the central region of the Sgr B2 M, being more evolved compared to Sgr B2 N, has spectral indexes close to 0, which is typical for optically thin HII regions. Considering the high density of HII regions in the same area described in Schmiedeke et al. (2016) we mark all previously uncategorized sources in the close vicinity as HII region candidates and give them a score of 0. Only a few sources are removed in Sgr B2 N with this method due to the high error values of the spectral index map in the region. We label the sources morphologically resembles HII regions (e.g. a source with a dim center but bright edges) as HII region candidates. Finally, we mark sources that are extremely bright at 3 mm as HII region candidates. Every HII region candidate that is not a previously known HII region, cannot be assigned to a previosly known HII region accounting for VLA’s poor absolute pointing accuracy, and is not a part of a “fragmented” known HII region is marked as a new HII region detection. In total, our catalog contains 17 known hyper-compact and ultra-compact HII regions, 21 HII region candidates, and 8 new hyper-compact HII regions.

Having two criteria for core identification, strict and lax, allows for separate “robust” and “complete” catalogs to co-exist. We note that the difference between a score of 1 and 2 is subjective. After performing the analysis described in the following section, we do not find any significant differences when comparing the results using the two catalogs. Thus, we report and use only the “complete” catalog in the rest of this work. Our catalog contains 371 cores at 3 mm and 222 cores at 1 mm, of which 168 have a 3 mm counterpart. Thus, the total number of individual cores identified at at least one wavelength is 425.

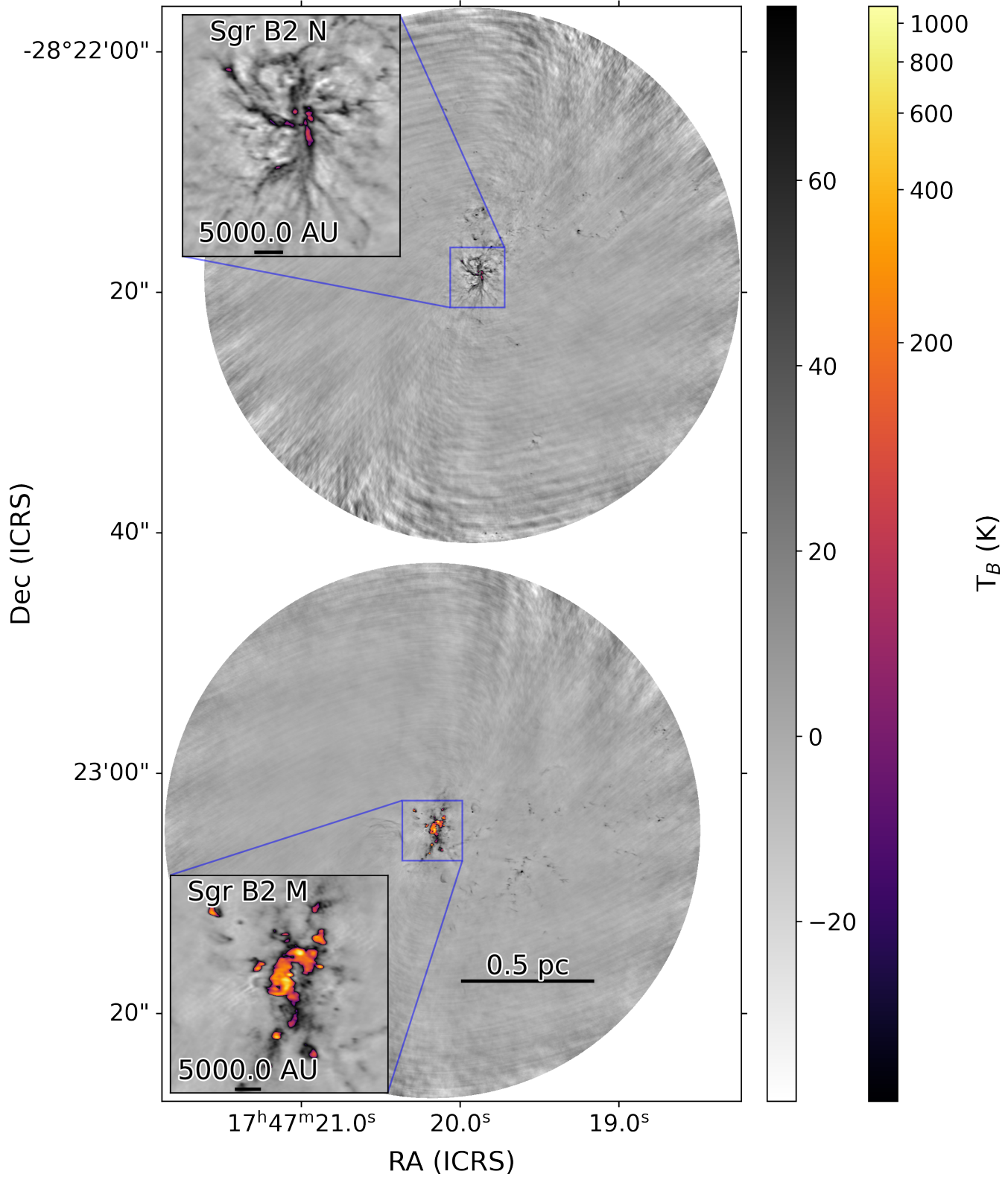


Figure 2. Band 6 (1 mm) continuum image of Sagittarius B2 N and M. Sgr B2 M appears to be hotter than Sgr B2 N. Due to the smaller field of view, Sgr B2 S and z that are visible in Band 3 are not present here.

The described approach has some caveats. Even after extensive self-calibration and cleaning, the data still include local artifacts such as negative bowls around bright sources and wave-like patterns on different scales. The high source density and the presence of extended emission (e.g. Figure 3), complicates the estimation of the local noise for each source.

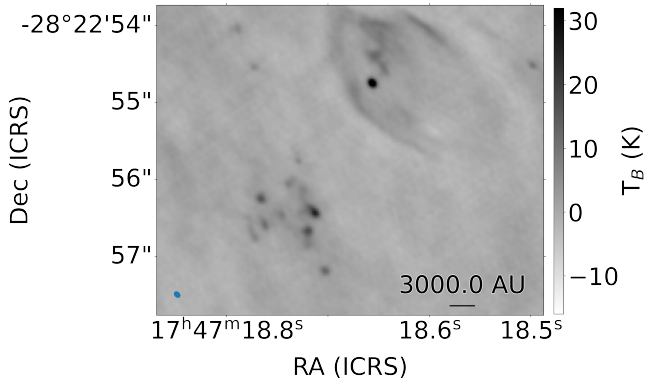


Figure 3. A zoom in on a region north-east from Sgr B2 M at 3 mm. It features H II region Sgr B2 Y from Schmiedeke et al. (2016) on the top-right, a core that is within the H II region’s projected area on the sky, and a highly-fragmented source on the bottom-left. This highly-fragmented group of ten detected cores was previously thought to be one massive core.

Excluding detections within polygons that were drawn by eye can potentially exclude true positives. While it is unlikely for cores to be present inside H II regions, they might appear to be so due to projection effects. Less than a few percent of the total pointing area is excluded by the polygons. Potentially missed sources should not affect the conclusions of this paper as there would be no biases for the excluded sources.

3.2. Photometry

We use the integrated flux within the dendrogram structure contour and the brightest pixel within the contour as the primary observables. We present the two measurements of source flux in the catalog in Table 3. The source brightness temperatures are shown in Figure 4 as a CDF.

The total source flux is the sum of the pixel values in Jy in the dendrogram-defined contour referred to as a “leaf”. The peak is the value of the brightest pixel in Jy/beam. These numbers are expected to be the same for a point source and the peak-derived value should be smaller for a resolved source. Dendrogram-based flux underestimates the flux of the very faint sources because the lowest possible contour is set at a given threshold level, in our case 4σ .

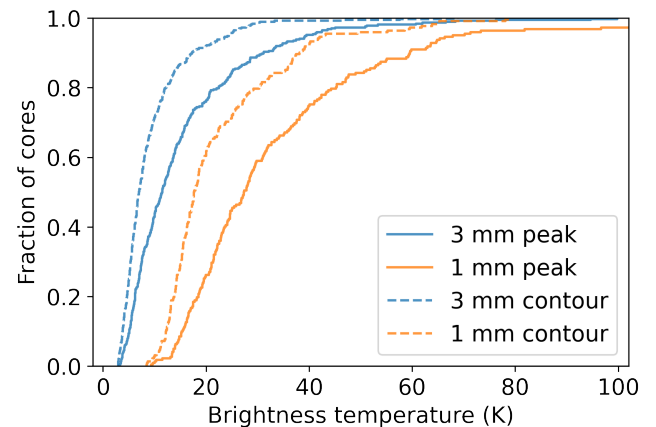


Figure 4. Brightness temperature of the cataloged cores. The brightness temperature is serves as a lower limit of the kinetic temperature for blackbody sources.

During testing, we attempted to perform 2D Gaussian photometry using the `gaussfit_catalog` python package. We inspected each fit by hand and found that fewer than 10% of the sources had a satisfactory fit for the central object. We found that many of the fits were affected by the presence of non-uniform extended envelopes around the centrally peaked sources, like in Figure 3. Furthermore, high source density and imaging artifacts also contributed to some of the failed fits. Thus, we concluded that our sources are not well-represented by simple 2D Gaussians and decided to use dendrogram contours to define sources.

3.2.1. Photometry comparison

As a part of Cycle 4 ALMA project 2013.1.00269.S, [Ginsburg et al. \(2018\)](#), hereafter G18) obtained Band 3 observations of the Sgr B2 cloud at 0.5" resolution.

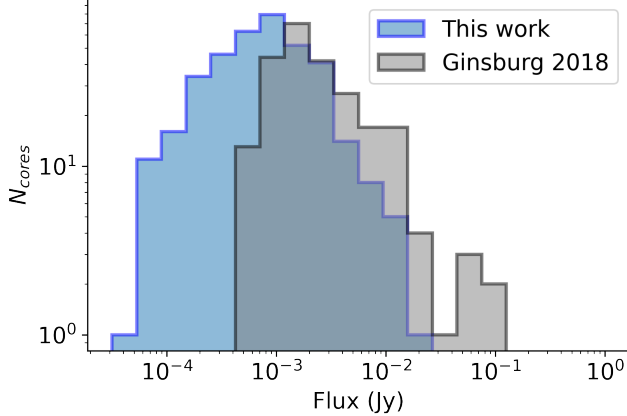


Figure 5. A comparison of our dendrogram contour-based, 3 mm source flux and the full 15×15 pc G18 catalog, with known HII regions removed from both data sets. The fluxes from G18 are divided by 0.92 to account for the difference in spectral setup assuming the sources have a spectral index of two. The general shape appears to be similar, but with the higher-resolution data, which have twice the sensitivity, we are able to detect fainter sources. The turnover point is at about 1 mJy, which is just below the turnover point in G18 catalog.

We investigate the impact of the differences between ours and G18 observations. Compared to G18, the catalog derived in this work has a factor of 10 better spatial resolution and is a factor of two more sensitive. The distribution of source fluxes is shown in Figure 5. The data from G18 were centered at 96.36 GHz with a bandwidth of 1.875 GHz, while our observations are centered at 92.45 GHz with the same bandwidth. Since the central frequencies of the data are not the same, we perform a frequency correction. Assuming that the majority of the flux within the G18 beam is coming from the optically thick part of the core or an HII region and it has an average spectral index of two, the

frequency correction factor is ~ 0.92 . For a positive spectral index, the flux measured from our data within the defined aperture is expected to be brighter. Depending on the source, the correction factor can range from 1.05 at spectral index of -1 to 0.87 at spectral index of 3.5 which would correspond to about 15% flux correction error. As shown in Section 3.4, many of the cataloged sources have spectral indexes between 2 and 3.

We compare our and G18 images by performing aperture photometry on G18 data. We apply an elliptical aperture equivalent to $1-\sigma$ of the G18 Gaussian beam ($0.230'' \times 0.197''$) on the locations of G18 detections on our data and compare it to the “peak” (brightest pixel) flux from G18. However, an elliptical aperture does not capture all the flux counted in the brightest pixel of an unresolved source. While the brightest pixel is representative of the sum of the Gaussian distribution of the signal, an elliptical aperture cuts off the edges of the distribution. We calculate the aperture correction factor as the fraction of the Gaussian distribution that is cut off after using a $1-\sigma$ -sized aperture to be 1.465. Finally, we convert the summed flux from Jy/beam to Jy. We compare this quantity with the brightest pixel of G18 sources. The ratio of flux at the location of each G18 source is shown in Figure 6. There is a slight trend of higher-resolution sources having less flux. A smaller fraction of sources are above the line. Low-flux sources exhibit larger scatter, which is consistent with measured noise. The somewhat large scatter can be partially explained by the presence of imaging artifacts in the images, primarily negative bowls.

3.3. Source sizes

For each source we recorded the total flux within the dendrogram object contour and the brightest pixel value within the contour. If a source is not resolved, then the brightest pixel should contain all the flux from the source. If a

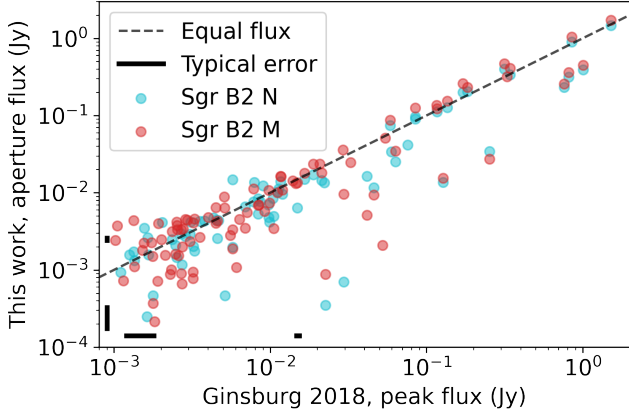


Figure 6. Aperture photometry comparison of our data and Ginsburg et al. (2018) data. Some scatter is present that can be explained by the difference in resolution, frequency, and the presence of imaging artifacts. The data points from Sgr B2 N and M that are almost identical are caused by the overlap in the two pointings’ field of view.

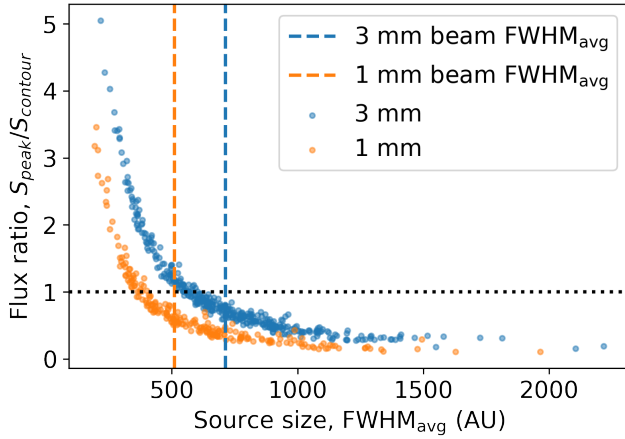


Figure 7. The ratio of the brightest pixel and the total source flux within dendrogram leaf structure is plotted against the average source FWHM as recorded by `astrodendro`. The flux ratios below one indicate likely resolved sources, which represent a majority in our sample.

source is resolved, the brightest pixel will contain only part of the flux. Thus, we use a ratio of brightest pixel flux and summed flux within dendrogram structure to serve as a metric of whether a source is resolved or not. As shown in Figure 7, we find that 20% of 1 mm and 30% of

3 mm sources have effective areas smaller than the beam area and peak flux larger than the dendrogram contour flux, which means that the sources are unresolved. On the other hand, only a handful of sources are more than two resolution elements across – 23 sources at 1 mm and 8 sources at 3 mm are well resolved.

The sources with $S_{peak}/S_{contour} < 1$ and dendrogram contour area larger than the beam size are marginally resolved. There are 45% of such sources at each wavelength.

3.4. Spectral indexes

The common beam between the two bands is equivalent to the Band 3 beam. Thus, we convolve the Band 6 data to the Band 3 beam, accounting for the beam area change as our data are in units of Jy/beam. To calculate the spectral index, we take the brightest pixel values for detections at 3 mm and take the corresponding positions on the sky at 1 mm. The brightest pixel contains information about at least the inner, most dense part of the source in its 2D projection. The mean offset between the locations of the brightest pixels at 3 mm and 1 mm is less than a quarter of the beam, which is equivalent to ~ 1 pixel and is never more than one common beam apart. We find that using the 1 mm data’s brightest pixel locations produces very similar individual measurements, much less than the calculated errors. We check for systematic errors that could be caused by this approach and find no trends in the measurements of the two distribution. In addition to calculating spectral indexes for sources present in both bands, we are also able to place upper and lower limits for sources detected only at 3 mm and 1 mm respectively. We show the distribution of spectral indexes with the corresponding source fluxes in Figure 8, indicating physical and observational constraints.

Since the flux measurements in two bands are uncorrelated distributions, we calculate the spectral index errors only for sources with SNR

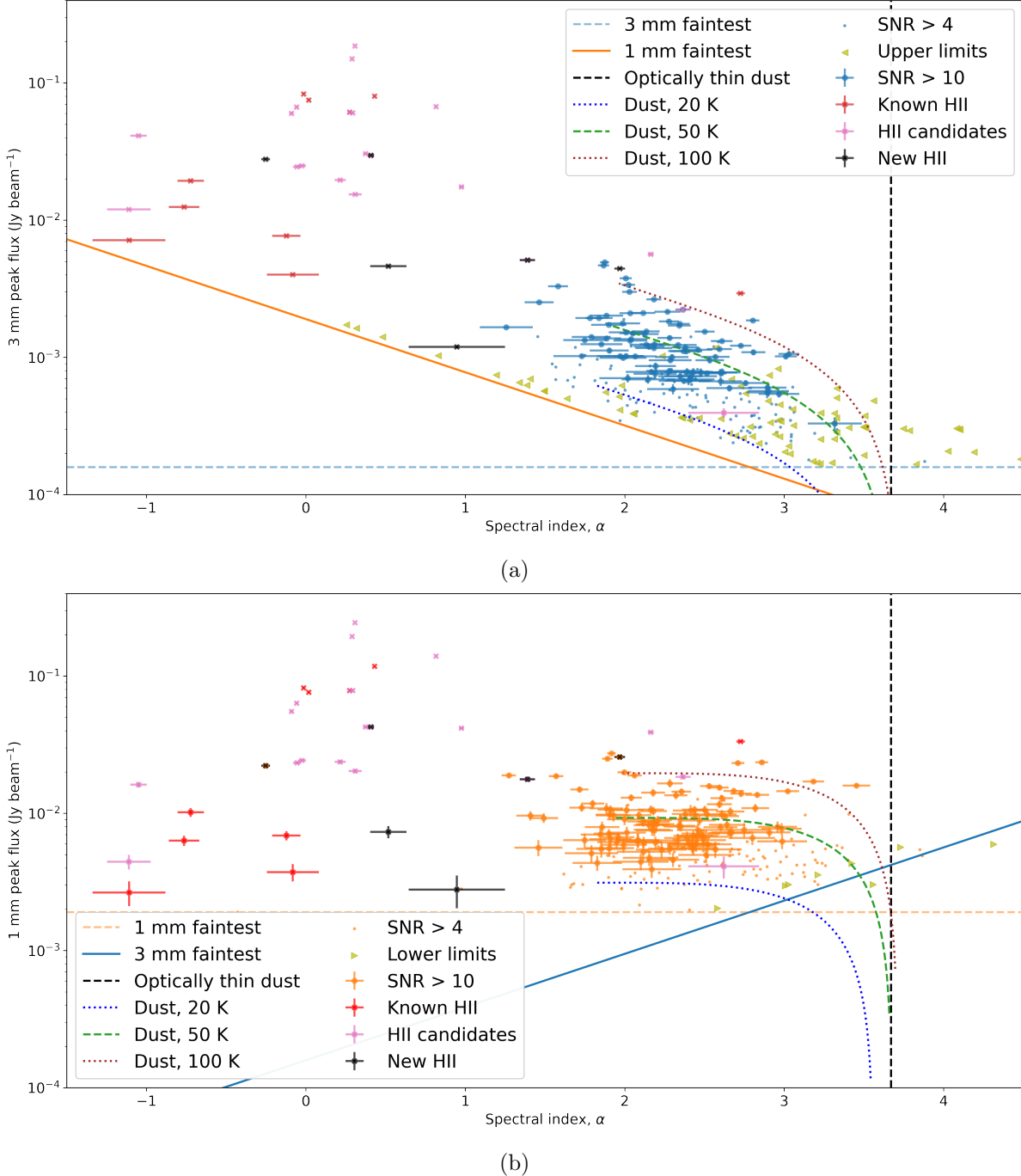


Figure 8. Source flux of 3 mm (a) and 1 mm (b) ALMA detections plotted against the calculated spectral index using the corresponding location at the other wavelength after matching beam sizes. Each line represents a physical or observational limit on possible values. We only calculate the errors of sources with signal-to-noise above 10, but all sources are shown for completeness. The 1 mm and 3 mm flux limits are based on the faintest detected source in the corresponding band. The dashed-green and dotted lines show the maximum flux at different temperatures of a source at different spectral indexes assuming the source is beam-sized. The detected sources fill the observable range completely. Follow up observations with higher sensitivities may reveal the missing dusty, optically thin sources. The olive triangles show the upper and lower limits on the spectral indexes for sources that have at least 4σ signal only in one band. The flux in the other band was taken as 4σ at that location in the image. The flux error bars are generally much smaller than the marker size and are only visible for low-flux sources.

over 10 in both bands. For sources with SNR below 10 in either band, the errorbars are not necessarily representative of the uncertainty because the error distribution function is no longer Gaussian (the distribution function for the ratio of two Gaussians with mean zero is a Cauchy distribution, for which the standard deviation and mean are undefined). We therefore show data points without error bars for these sources in Figure 8. All sources in our catalog have the SNR > 4.

Convolving Band 6 data to the common beam results in a factor of two decrease in SNR for compact sources, which leaves only a few sources with SNR above 10 and significantly decreases the number of sources with SNR > 4. Assuming that the radial brightness profile of the sources is the same, convolving data to a larger beam would increase the source flux measurements by the same factor. The resulting flux distribution of sources with the new, lower SNRs would be scaled, but have a similar shape. Thus, we use the original SNR, before data convolution, to perform the 10σ and 4σ cuts. We then use the convolved data to calculate individual source errors

We investigated whether we could use the alpha-maps produced by the `tclean` algorithm to estimate the in-band spectral indexes. Fewer than a dozen sources had errors below 50%. Thus, our data is not sensitive enough to produce in-band spectral indexes.

We explore the potentially misclassified sources in our catalog. The “core” classification was done based on the morphology, proximity to other sources, relative brightness, and surrounding emission. The spectral index values can then be used to identify potential catalog contaminants such as H II regions. As shown in Figure 9, there are five sources that have statistically significant spectral indexes below 2, which are probably misclassified H II regions. However, at least three of these sources are lo-

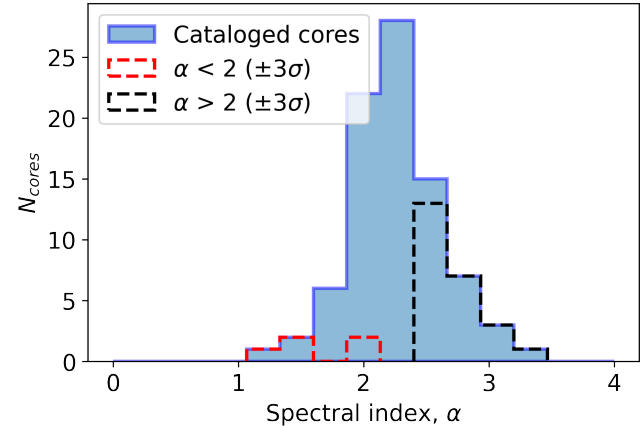


Figure 9. Spectral indexes of the sources in our catalog. We cross-matched 92.45 GHz and 225.78 GHz detections and calculated the spectral indexes as described in Section 3.4. We exclude any source that has the a continuum signal-to-noise below 10 in either band. The red dotted histogram shows the sources that have been cataloged as “cores” that have statistically significant ($\pm 3\sigma$) spectral index below 2. The black dotted histogram shows the fraction of sources that are not completely optically thick and have the calculated spectral index above 2.

cated in the negative bowls in Band 6 data. Since our catalogued fluxes are not background subtracted, being located in the negative bowl causes a lower 1 mm flux and underestimates the spectral index. Similarly, being located in a negative bowl at 3 mm artificially increases the spectral index. A known H II region Sgr B2 F10.30 is the most prominent example of a source in a 3 mm negative bowl, having $\alpha = 2.7$. Thus, some of the detections near negative bowls might have been misclassified; as shown in Figure 8, there are some H II region candidates that have $\alpha > 2$ and cores with $\alpha < 2$. Fewer than 1% of sources are located in a vicinity of negative bowls.

We also note that just above 60% of our 3 mm detections fall within the field-of-view of 1 mm pointings. We extrapolate the derived spectral-index-based conclusions to the rest of the 3 mm sources. While the distance from the central

regions of the clusters might have some impact on core temperature and age, it does not impact the conclusions of this paper.

3.5. Source masses

Using a number of assumptions about the properties of a core, including that the dust is optically thin, we can derive the mass of such a core. We start from a modified blackbody equation:

$$F_\nu = \pi \frac{2h\nu^3}{c^2} \left(1 - e^{h\nu/k_B T}\right)^{-1} (1 - e^{-\kappa_\nu \Sigma}), \quad (1)$$

where F_ν is the spectral flux density, h is the Planck constant, ν is the frequency, c is the speed of light, k_B is the Boltzmann constant, κ_ν is the dust opacity index and Σ is the surface density. Given an area A , the mass M is

$$M = \Sigma A. \quad (2)$$

We can apply the optically thin dust assumption ($\kappa_\nu \Sigma \ll 1$) and solve for the mass:

$$M = \frac{S_\nu d^2}{B_\nu \kappa_\nu}, \quad (3)$$

where S_ν is the flux density, d is the distance to Sgr B2, and B_ν is the spectral brightness. Or, adopting the Rayleigh-Jeans approximation and expressing in terms of brightness temperature:

$$M = \frac{T_B d^2}{\kappa_\nu T_{KE}}, \quad (4)$$

where T_B is the brightness temperature and T_{KE} is the kinetic temperature of the source. Extrapolating the Ossenkopf & Henning (1994) opacity models for dust grains with thin ice mantles, gas density of 10^6 cm^{-3} , and age of 10^5 years as a power law, assuming $\beta_{\text{dust}} = 1.75$, we obtain $\kappa_{92\text{GHz}} = 0.0017 \frac{\text{cm}^2}{\text{g}}$ and $\kappa_{226\text{GHz}} = 0.0083 \frac{\text{cm}^2}{\text{g}}$. Further assuming a uniform core temperature $T_{KE} = 50 \text{ K}$ and a distance³ of 8.4

kpc we obtain source masses shown in Figure 10.

Since the cores are at least partially optically thick, we can obtain only a lower limit on their dust masses. Other variables being constant, an optically thick source contains more mass than an optically thin source. Here, we utilize the

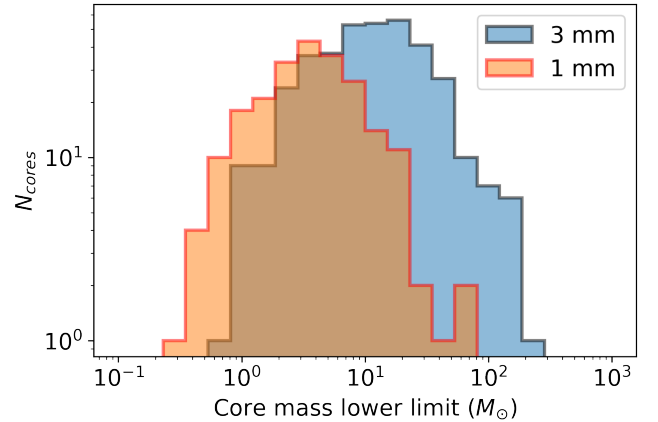


Figure 10. The inferred lower mass limit of the sources using the optically thin dust assumption for 1 mm and 3 mm data. 1 mm data has a higher mass sensitivity that is caused by the dust becoming more optically thick at higher frequencies and thus lower mass sources can be detected. We assume a uniform dust temperature of 50 K and a gas-to-dust ratio of 100.

total dendrogram flux instead of the source's brightest pixel value to account for the sources that are partially resolved. Such a method noticeably underestimates the masses of faint sources, as our run of `astrodendro` algorithm cuts off every part of the source that is below 4σ .

Both the individual mass measurements and mass distributions based on the 1 mm and 3 mm observed flux do not match. We attribute this to the erroneous assumption of optically thin dust used for this calculation. Such an assumption underestimates the masses at 1 mm more than at 3 mm as dust has longer mean free path at longer wavelengths and thus flux is emitted from more of the material before reaching op-

³ Using the most recently measured distance of 8.127 kpc (GRAVITY Collaboration et al. 2018) would result in 7% lower masses.

tically thick regime. Thus, we use the masses based on the 3 mm data as the lower limits in the rest of the paper.

Importantly, the temperature of cores is not uniform and can theoretically have any value. Still, using 50 K as a representative temperature can give us some understanding of possible mass ranges and show the general shape of the core mass distribution.

As shown by Bonfand et al. (2019), some cores can have average temperatures close to or above 150 K, usually referred to as hot cores. We detect sources at the locations of at least several such hot cores. Such sources are most likely the hot cores’ central disks as our largest recoverable scale of ~ 7500 AU is on the lower side of the typical hot core sizes (Jeff et al., in prep). At such high temperatures, the ice mantles surrounding the dust will start to sublimate. Such physical changes would decrease the emissivity by a factor of a few. At the same time, it is not clear how this affects the gas-to-dust ratio.

4. DISCUSSION

4.1. Nature of the observed sources

4.1.1. Protostellar cores: Stage 0/I YSOs

Our “core” catalog consists primarily of compact dusty sources with sizes between 200 AU and 1000 AU. Based on basic modeling, we show in this section that our cores are most consistent with an average temperature ~ 50 K. Such objects are, given the lower limit on their densities, unlikely to be in pressure equilibrium. We therefore identify these as rotationally-supported disks consistent with Stage 0/I YSOs⁴. We show the arguments in favor of this conclusion below.

In contrast to many studies of cores in nearby star-forming regions that assume a constant

disk temperature of 20 K to make consistent comparisons between the works (e.g., Eisner et al. 2018; Otter et al. 2021) we show that the core temperatures in Sgr B2 are more consistent with $T = 50$ K. Average dust temperatures based on *Herschel* line-of-sight observations (Etalaze et al. 2013) and theoretical models of external dust heating due to stars (Schmiedeke et al. 2016) both produce ~ 20 K average temperature in the moderate-density dust ($n \lesssim 10^5$ cm $^{-3}$) in Sgr B2 region. However, the denser regions have gas temperatures that are substantially higher (e.g., Ginsburg et al. 2016; Krieger et al. 2017). The modeled dust temperatures towards the centers of Sgr B2 N and M can go as high as 350 K and 600 K respectively (Schmiedeke et al. 2016). Since we are observing cores, which are local overdensities, we expect temperatures higher than 20 K.

If we assume, very simplistically, that all of our observed cores are optically thick beam-sized spheres, about 50% of the cores at 3 mm and fewer than 20% of the cores at 1 mm are consistent with temperatures below 20 K, as shown in Figure 11. In reality, it is extremely unlikely that all of the cores are close to beam-sized. Sources smaller than the beam size would need to be warmer to produce the same flux. Furthermore, Figure 8 shows that most of the cores are not completely optically thick, which requires the assumed temperatures to be even higher. About 75% of 1 mm detections are consistent with average temperatures of at least 50 K with the remaining 25% being hotter. Thus, in this work we take the average core temperature to be 50 K.

To test our assumptions, we create a simple model of our observed sources. It consists of an optically thick sphere of radius R that is surrounded by optically thin dust of a certain surface density. This model mimics a face-on optically thick disk embedded in dust and is intended to confirm that we are able to detect

⁴ We extrapolate the original luminosity-accretion-based definition of stages for low-mass sources to their high-mass analogues from Robitaille et al. (2006).

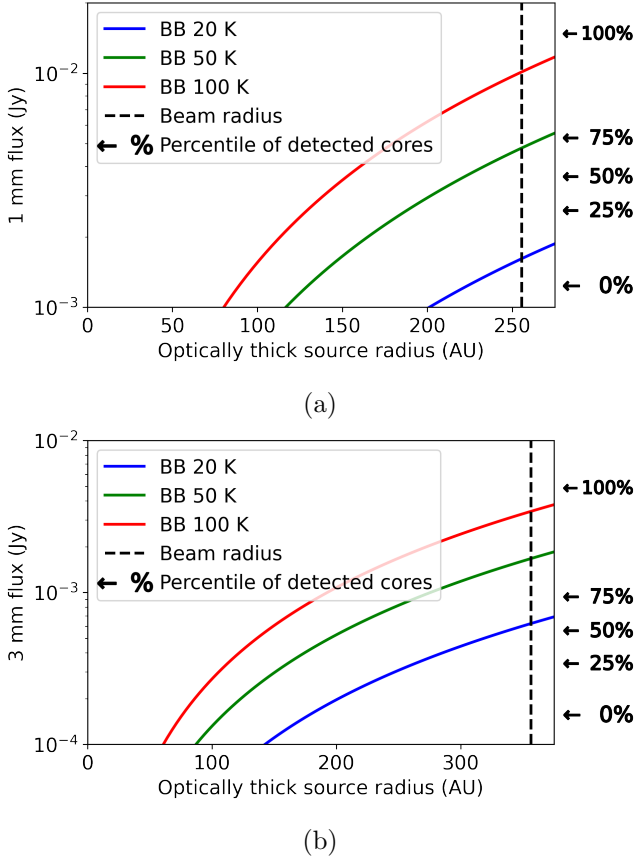


Figure 11. A model of an optically thick (blackbody) source within our beam at 1 mm (a) and 3 mm (b). By changing the size of the optically thick sphere we can see how many of the sources in our core catalog can be explained using this model. Assuming a beam-sized or larger optically thick core, less than 20% of the 1 mm detections can be explained by core temperatures of 20 K. If some of the sources are smaller and are not completely optically thick, the average temperature would have to be even higher. Thus, we assume a higher average core temperature of 50 K.

dusty disks. Since many of our sources are calculated to be slightly optically thick, we also use this to test the expected spectral indexes for optically thick sources embedded in optically thin dust.

Assuming a gas-to-dust ratio of 100, we represent the dust surface density using gas column density, with an average over the Sgr B2 N and M cluster of around $3 \times 10^{24} \text{ cm}^{-2}$ (Sánchez-Monge et al. 2017). As discussed above, we

assume a dust temperature of 50 K. Figure 12 shows the expected spectral indexes of such sources as a function of the radius of the central optically thick sphere and the gas surface number density. We further indicate the region on the plot that will not be detectable in either of our bands at our sensitivity as the white-out region on the bottom left. The unshaded region of the plot corresponds to the parameters of our simplified model that can explain the observed sources.

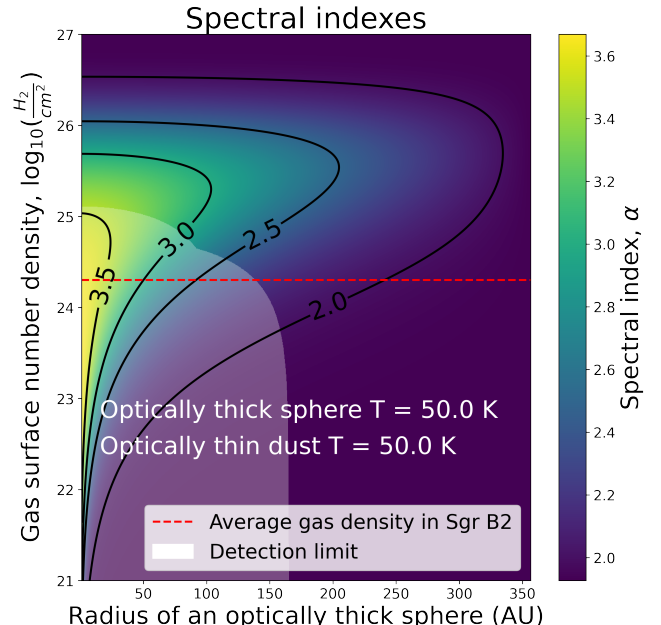


Figure 12. Modeled spectral indexes for an optically thick spherical core of a certain radius surrounded by optically thin isotropic dust of a given gas surface number density. A gas-to-dust ratio of 100 is assumed. The average gas surface density of $3 \times 10^{24} \text{ cm}^{-2}$ in Sgr B2 (Sánchez-Monge et al. 2017) is most likely representative of the minimum gas surface density within our beam centered on our detections. We do not expect any sources to be below this line, since all detections represent overdensities. The spectral index of an optically thick blackbody at 50 K is close to 1.93. The white shaded area indicates a parameter space of sources below our data's sensitivity.

Using this model, for an optically thick face-on disk with an average temperature of 50 K we

conclude that: a) in lower column density regions ($< 10^{24} \text{ cm}^{-2}$) we are sensitive to sources that are larger than $\sim 300 \text{ AU}$ in diameter and b) as the density increases past the average density in Sgr B2 (and up to 10^{26} cm^{-2} where the surrounding dust becomes optically thick) the optically thin dust becomes the dominant source of emission.

The sources in our catalog are also much brighter than in any of the nearby star-forming regions. In the Orion molecular cloud only four of the brightest disks would be detectable at Sgr B2's distance (Tobin et al. 2020). Only a few of the disks in Orion are larger 200 AU with corresponding masses $0.2 M_{\odot}$. The sources in our catalog are most likely larger, more massive, and warmer than the ones in Orion.

4.1.2. HII regions

We evaluate whether the sources with $\alpha \approx 2$ could be HII regions and conclude that they are most likely not. Given typical physical parameters for HII regions in Sgr B2, it is possible, however unlikely, for many of our sources with spectral indexes of 2 to be such HII regions. At brightness temperatures of 10^4 K , in order to match the range of recorded fluxes in our catalog, an optically thick HII region would have to be between 30 AU and 80 AU in diameter. Using a Strömgren sphere as an approximation, we find that such hyper-compact HII regions can potentially exist in densities between 10^7 and 10^9 cm^{-3} , which are reasonable densities for Sgr B2. However, any optically thick HII region larger than 80 AU in diameter would be detected with our sensitivity. No such sources are present in our catalog. Roughly 100 sources in our catalog have $\alpha \approx 2$. By making several assumptions, such as higher HII region metallicity (which will lower its electron temperature) and the right amount of high-mass stars embedded in higher-than-previously-measured gas densities, many of the observed optically thick sources can be attributed to 30-80 AU HII re-

gions. At the same time, there exists a population of HII regions larger than 500 AU (e.g. this work, Meng et al. 2022). Assuming that the HII regions evolve continuously, the absence of 80-500 AU scale HII regions indicate that there was an abrupt period with no stars being formed. A short, temporary, and complete interruption of star-forming processes would be extremely unusual. Thus, we claim that there are very few to none HII regions contaminating our catalog. Additional observations, e.g. radio recombination lines, could help determine the nature of these sources definitively.

4.1.3. Prestellar cores

As described in Section 3.5, we can place a lower limit on the masses of our sources by assuming each is a beam-sized uniform sphere with a dust optical depth of 1. Free-fall time of a spherically-symmetric core is:

$$t_{ff} = \sqrt{\frac{3\pi}{32G\rho}} = \sqrt{\frac{3\pi V}{32Gm}} = \sqrt{\frac{\pi^2 R^3}{8Gm}}, \quad (5)$$

where G is the gravitational constant and V , m , and R are the volume, mass, and radius of a0 core. Taking the least massive source in our catalog ($\sim 1 M_{\odot}$) to be beam-sized (*sim* 700 AU) would result in free-fall times of 1200 years, while the most massive core of the same size would have a free-fall time of 40 years – extremely short on star formation scales. Thus, it is unlikely that any of our sources (at least on $\sim 600 \text{ AU}$ scales) are still undergoing free-fall collapse, indicating that there are no prestellar cores in our sample. While this is an extreme approximation, the higher mass, heterogeneous nature of the source, and the influence of the surrounding environment would speed up the infall of the material.

We can further estimate the effects of the high-pressure environment using the Bonnor-Ebert mass:

$$1.18 \frac{c_s^4}{G^{3/2} p_{BE}^{1/2}}, \quad (6)$$

where c_s is the speed of sound, 0.4 km/s ($T = 50$ K), G is the gravitational constant, and p_{BE} is the pressure ($P/k_B = 10^8$ K cm $^{-3}$) (Myers et al. 2022). The maximum Bonnor-Ebert mass for the sources in the CMZ is then $\sim 1 M_\odot$. Only two cores in our catalog have mass lower limits below $1 M_\odot$. Thus, the majority of the cores are not pressure supported. Having ruled out the free-fall collapse and pressure support, and the improbable magnetic field support, the remaining option is the rotational support of disks.

4.1.4. Stage II and III YSOs

With a dust mass lower limit of the catalogued sources, we can approximate the masses of the central stars for Stage II YSOs. We extrapolate the ratio of the dust mass and the central star of $\sim 1\%$ (Williams & Cieza 2011) one order of magnitude to calculate the possible mass of the central star for the least massive sources in our catalog. The faintest source in our data is 1.2 mJy at 1.3 mm, which would correspond to a central star with a mass of at least $30 M_\odot$. If all of our observed sources are Stage II YSOs, the median star mass would be around $300 M_\odot$, which is on the order of the largest stars ever detected. Current disk demographic samples (e.g., Andrews et al. 2018; Williams & Cieza 2011) are limited to $M \lesssim 2 M_\odot$. Finally, if we assume an optically thick, face-on dusty disk with an average temperature of 50 K, the disk would have to be at least 200 AU in size to be detectable with our sensitivity. All of our targets, if they are disks, must be larger and more massive than any disks observed in the local neighborhood (e.g., Andrews et al. 2018). Stage III YSOs do not have infrared excess and thus could not possibly be detected in our data.

4.2. Inferred stellar mass

We augment the method described in G18 to calculate the inferred stellar mass for each cluster. We use the core mass calculations from Section 3.5 to calculate the potential stellar mass

assuming that roughly one third of a core mass will end up in a star (Lada & Lada 2003). We take 6σ as our completeness limit – 0.3 mJy for Sgr B2 M and 0.2 mJy for Sgr B2 N, which corresponds to $1.5 M_\odot$ and $1 M_\odot$ stellar mass respectively. We exclude all the sources below this completeness limit. Following the clusters’ extent used in Schmiedeke et al. (2016), we take the radii of Sgr B2 N and M clusters to be 0.4 pc and 0.5 pc, respectively. We then assume that each H II region is powered by a $> 20 M_\odot$ star. We count the number of H II regions within each cluster from De Pree et al. (1998) and Meng et al. (2022). We assume a Kroupa initial mass function (Kroupa 2001) to perform the following estimates. The average mass of the stars powering the H II regions is $45 M_\odot$. Combining the core-based stellar mass with the H II region-based stellar mass we infer the total stellar mass by extrapolating for the stars below our completeness limit. Following the arguments outlined in G18, we estimate the star formation rate (SFR) for each cluster, taking the age of the cloud as 0.74 Myr (Kruijssen et al. 2015). The results and comparison with previous works are shown in Table 2.

With the high-resolution data, it is evident that the historically defined sizes of Sgr B2 Main and North in Goldsmith et al. (1990) do not necessarily represent which sources are part of the clusters. Both N and M have a continuous “chain” of sources in projection in the eastward direction, as visible in Figures 1 and 2. The defined sizes split these “chains” of sources. Further kinematics studies of the region, similar to, that extended beyond the centers of the clusters (e.g. Schwörer et al. 2019) are needed to determine which sources belong to which protocluster and would allow for more accurate count-based cluster mass estimation.

We use the variability of inferred total stellar mass as a function of assumed catalog mass completeness limit, like shown in Figure 13, to

Table 2. Inferred stellar mass of Sgr B2 N and M using source counting. Using the calculated core mass, we estimate the core-based stellar mass (M_{count}). We assume a lower completeness limit to be $1.5 M_{\odot}$ in stellar mass and use Kroupa IMF (Kroupa 2001) to infer the stellar mass ($M_{inferred,core}$). We assume that each H II region contains a $45 M_{\odot}$ star to infer the $M > 20 M_{\odot}$ tail of the IMF. Combining the direct counting of cores and H II regions, we infer the total stellar mass in each cluster ($M_{inferred,total}$). The star formation rate assumes $t_{SF} = 0.74$ Myr.

Name	M_{count} (M_{\odot})		$M_{inferred,core}$ (M_{\odot})		$M_{inferred,total}$ (M_{\odot})		SFR ($M_{\odot} \text{ yr}^{-1}$)	
	This work	G18	This work	G18	This work	G18	S16	
N	960	270	5900	1500	2300	1200	2400	0.0031
M	490	2300	5100	2300	6300	8800	20700	0.0085

make a conjecture on the shape of the IMF. Let an observed cluster have a Kroupa IMF. Assuming that the observationally-derived masses match the actual masses of the cores, as long as we choose an assumed completeness above the “true” completeness, the Kroupa-IMF-based total inferred stellar mass will remain the same. This would show up as a horizontal line on Figure 13. If we pick a mass completeness limit below the “true” completeness, we will underestimate the total mass.

Now, assume that the observed cluster has a high-mass star excess (i.e. shallower IMF). If we repeat the same exact process of inferring the total stellar mass assuming a “normal” Kroupa IMF, we will consistently overestimate the total mass. Moreover, the larger the assumed completeness limit we choose, the more the mass will be overestimated. This would correspond to a line with an upward trend on Figure 13. The inferred stellar mass as a function of assumed completeness limit for this work appears to have such an upward trend, which could be indicative of a shallower IMF.

Here I intend to include a couple paragraphs discussing what would need to happen so that our observed core mass function turns into a Kroupa IMF by challenging the assumptions made in this paper:

1. Systematic core temperature variation (are larger cores hotter?)

2. Systematic star formation efficiency variation (do massive cores convert less of their mass into stellar mass?)
3. Varying binary function (do high-mass cores form more binaries than low-mass cores?)
4. Systematic accretion rate variation (will the low-mass cores accrete more material than the high-mass cores when they reach the IMF?)

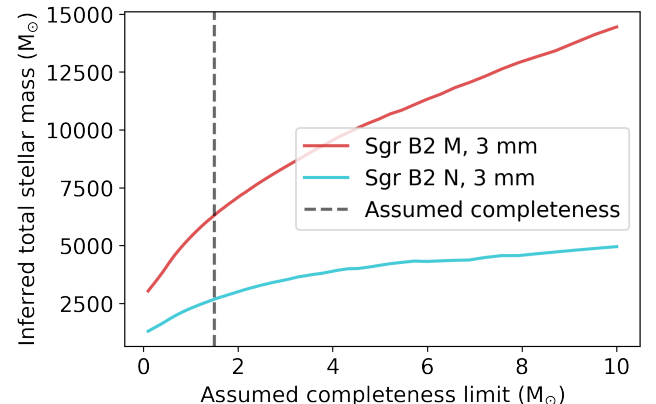


Figure 13. Inferred total stellar mass for Sgr B2 N and M as a function of the assumed completeness mass limit in our data. The assumed completeness for the calculations shown in Table 2 is taken at 6σ and converted to star mass equivalent assuming optically thin dust and a 30% star formation efficiency and is shown as a dashed line.

4.3. Core fragmentation

We compare our core catalog with G18, which observed Sgr B2 N and M at 10 times coarser resolution. For each low-resolution detection, we find the number of high-resolution detections within $1.5 \times$ beam FWHM of the source center. We exclude sources from the G18 catalog that would not be detectable in our data, specifically at the pointing edges where the sensitivity is lower. Out of 371 detections at 3 mm in our catalog, 109 cores are contained within the fragmented low-resolution sources, 42 are one-to-one match, and the remaining 220 are new detections with no corresponding detections in G18.

Our shortest baseline length of 41 m is longer than the 15 m in G18 data. On average, our images are made weighting longer baselines on average. As the result, some of the previous detections are resolved out. We find that over half of the low resolution detections “fragment” into two or more sources, with one of the sources fragmenting into ten, as shown in Figure 3. We also find that over a dozen sources from the low-resolution catalog do not have a counterpart in the high-resolution catalog. The distribution is shown in Figure 14. We do not find any pattern in the locations of the cores that fragment vs those that do not. Figure 15 shows the spatial distribution of the cross-matched and resolved-out sources as well as the new detections.

The high-resolution data’s largest recoverable scale is $0.9''$, or ~ 7500 AU. While some faint and extended sources might indeed have been resolved out, at least some of the low-resolution detections are likely false positives due to imaging artifacts.

On average, each detected G18 source fragments into 2 cores. If we take the one third of the sources that fragment, then there is an average of 3.4 cores per G18 fragmenting source. In general, source fragmentation changes the shape of the core mass function (and if these fragments

represent individual systems – the IMF), making it less steep. Because cores previously inferred to contain single very massive stars are broken into many lower-mass objects, increasing the total number of sources, which significantly reduces the total expected luminosity.

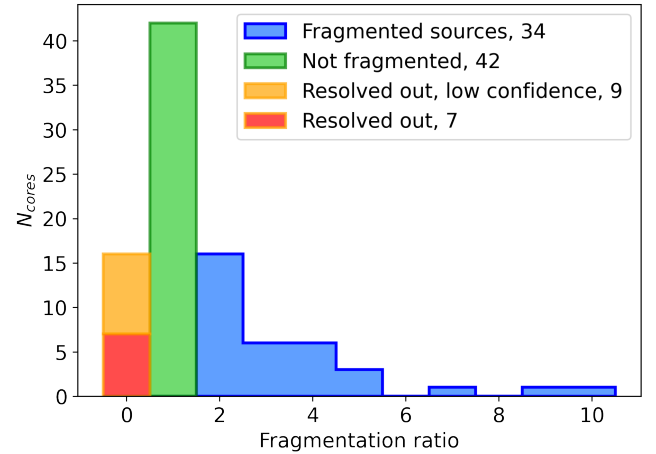


Figure 14. Number of sources from our data that fall within $1.5 \times$ FWHM of G18 sources. Over 50% of the G18 sources fragment into two or more sources. The left-most bin shows sources from G18 that do not have a counterpart in our data. On average, each G18 source fragments into two.

5. SUMMARY

We presented ~ 700 AU follow-up continuum observations of a massive molecular cloud in the CMZ – Sagittarius B2. We detected 425 unique cores: 371 at 3 mm, a twofold increase, and 222 at 1 mm. Most of the newly detected sources are due to the increased sensitivity, while about a fifth come from resolving fragmented sources. We find most sources to be marginally resolved and have a spectral index consistent with $2 < \alpha \lesssim 3$. We infer that the dusty objects we observe must be warmer than disks observed in the Galaxy. Because of their high temperatures, these sources are unlikely to be prestellar cores. Because of their high column densities, they are unlikely to be Stage II or later YSOs. We therefore conclude

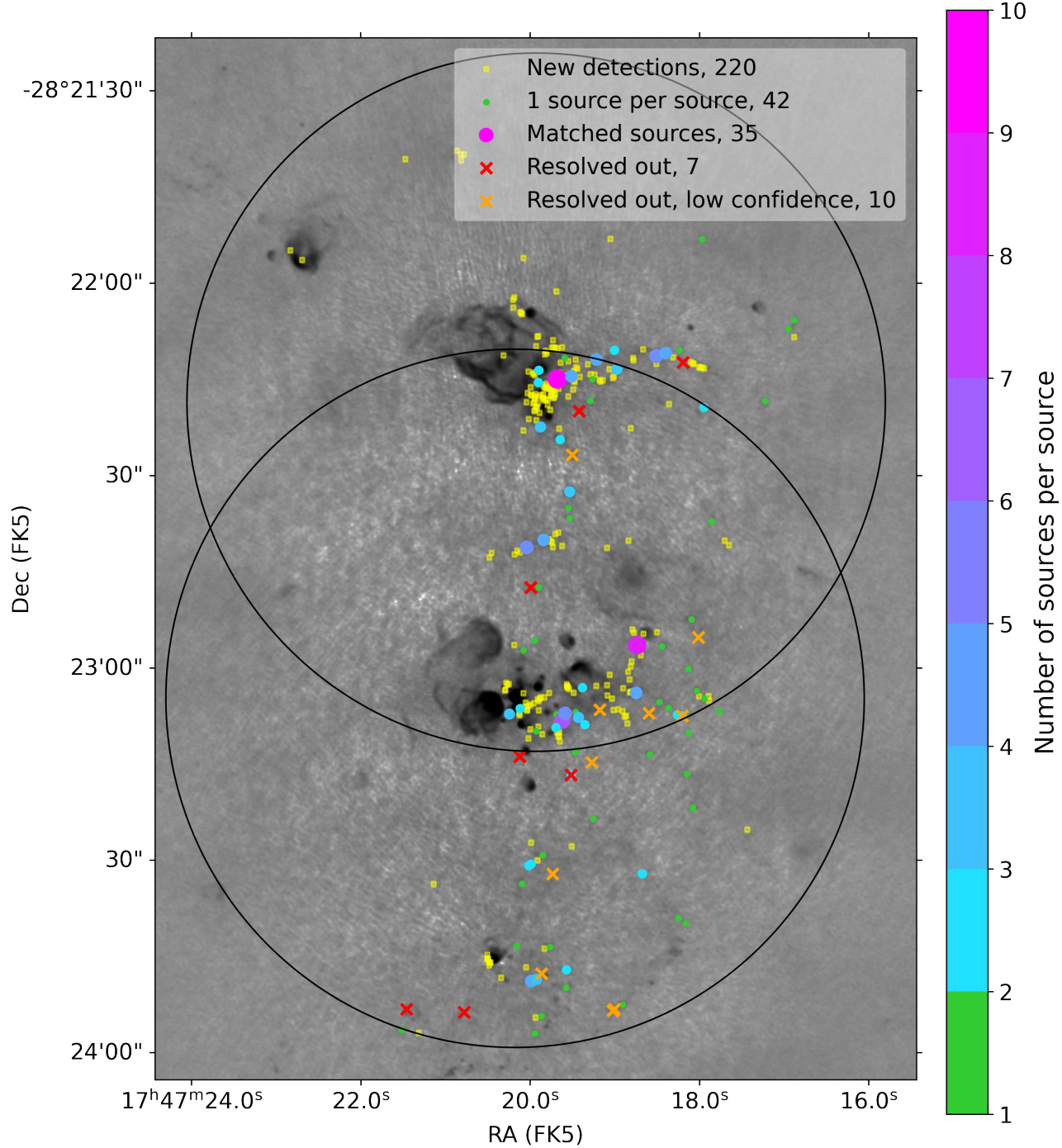


Figure 15. 3 mm ALMA mosaic of Sgr B2 adapted from [Ginsburg et al. \(2018\)](#). The black circles show the field of view of the two 3 mm pointings in this work. The filled-in circles show the sources that have been matched by-hand between the two data sets, with H II regions disregarded. The color and the size of the circles show the number of higher-resolution sources within $1.5 \times \text{FWHM}$ of the lower resolution beam, which we interpret as fragmentation. The x's indicate sources resolved out with the increase in resolution and increase in the shortest baseline length. “Low confidence” detections from [Ginsburg et al. \(2018\)](#) are shown in orange. The detections visible in the figure but not marked are either H II regions or are located at the edge of the high-resolution pointings where the sensitivity was below the detection threshold for such sources. Some of the “resolved out” sources (including the red high-confidence detections) are likely to be false detections caused by imaging artifacts.

that the sample is comprised primarily of Stage 0/I YSOs. Using direct source counting, we infer the total stellar mass of $2300 M_{\odot}$ for Sgr B2 N and $6300 M_{\odot}$ for Sgr B2 M. The resulting star formation rate is $0.0031 M_{\odot} \text{ yr}^{-1}$ for Sgr B2 N and $0.0085 M_{\odot} \text{ yr}^{-1}$ for Sgr B2 M.

ACKNOWLEDGMENTS

This paper makes use of the following ALMA data: ADS/JAO.ALMA#2016.1.00550.S, ADS/JAO.ALMA#2013.1.00269.S. ALMA is a partnership of ESO (representing its member states), NSF (USA) and NINS (Japan), together with NRC (Canada), MOST and ASIAA (Taiwan), and KASI (Republic of Korea), in cooperation with the Republic of Chile. The Joint ALMA Observatory is operated by ESO, AUI/NRAO and NAOJ. The National Radio

Astronomy Observatory is a facility of the National Science Foundation operated under cooperative agreement by Associated Universities, Inc. AG acknowledges support from the NSF under CAREER 2142300 and AST 2008101 and 2206511.

Facilities: ALMA

Software: Image reduction and final catalogs are available on GitHub: https://github.com/bazarsen/SgrB2_ALMA_continuum. This work utilized the following tools: `astropy` (Astropy Collaboration et al. 2013, 2018), `CASA` version 5.7.0-134.el7 (McMullin et al. 2007), `astrodendro` (Rosolowsky et al. 2008), `dendrocat`, `radiobeam`.

REFERENCES

- Andrews, S. M., Huang, J., Pérez, L. M., et al. 2018, ApJL, 869, L41, doi: [10.3847/2041-8213/aaf741](https://doi.org/10.3847/2041-8213/aaf741)
- Astropy Collaboration, Robitaille, T. P., Tollerud, E. J., et al. 2013, A&A, 558, A33, doi: [10.1051/0004-6361/201322068](https://doi.org/10.1051/0004-6361/201322068)
- Astropy Collaboration, Price-Whelan, A. M., Sipőcz, B. M., et al. 2018, AJ, 156, 123, doi: [10.3847/1538-3881/aabc4f](https://doi.org/10.3847/1538-3881/aabc4f)
- Barnes, A. T., Longmore, S. N., Battersby, C., et al. 2017, MNRAS, 469, 2263, doi: [10.1093/mnras/stx941](https://doi.org/10.1093/mnras/stx941)
- Bonfand, M., Belloche, A., Garrod, R. T., et al. 2019, A&A, 628, A27, doi: [10.1051/0004-6361/201935523](https://doi.org/10.1051/0004-6361/201935523)
- De Pree, C. G., Goss, W. M., & Gaume, R. A. 1998, ApJ, 500, 847, doi: [10.1086/305782](https://doi.org/10.1086/305782)
- Eisner, J. A., Arce, H. G., Ballering, N. P., et al. 2018, ApJ, 860, 77, doi: [10.3847/1538-4357/aac3e2](https://doi.org/10.3847/1538-4357/aac3e2)
- Etxaluze, M., Goicoechea, J. R., Cernicharo, J., et al. 2013, A&A, 556, A137, doi: [10.1051/0004-6361/201321258](https://doi.org/10.1051/0004-6361/201321258)
- Gallego-Calvente, A. T., Schödel, R., Alberdi, A., et al. 2022, A&A, 664, A49, doi: [10.1051/0004-6361/202141895](https://doi.org/10.1051/0004-6361/202141895)
- Ginsburg, A., & Kruijssen, J. M. D. 2018, ApJL, 864, L17, doi: [10.3847/2041-8213/aada89](https://doi.org/10.3847/2041-8213/aada89)
- Ginsburg, A., Henkel, C., Ao, Y., et al. 2016, A&A, 586, A50, doi: [10.1051/0004-6361/201526100](https://doi.org/10.1051/0004-6361/201526100)
- Ginsburg, A., Bally, J., Barnes, A., et al. 2018, ApJ, 853, 171, doi: [10.3847/1538-4357/aaa6d4](https://doi.org/10.3847/1538-4357/aaa6d4)
- Goldsmith, P. F., Lis, D. C., Hills, R., & Lasenby, J. 1990, ApJ, 350, 186, doi: [10.1086/168372](https://doi.org/10.1086/168372)
- GRAVITY Collaboration, Abuter, R., Amorim, A., et al. 2018, A&A, 615, L15, doi: [10.1051/0004-6361/201833718](https://doi.org/10.1051/0004-6361/201833718)
- Henshaw, J. D., Longmore, S. N., Kruijssen, J. M. D., et al. 2016, MNRAS, 457, 2675, doi: [10.1093/mnras/stw121](https://doi.org/10.1093/mnras/stw121)
- Hosek, Matthew W., J., Lu, J. R., Anderson, J., et al. 2019, ApJ, 870, 44, doi: [10.3847/1538-4357/aaef90](https://doi.org/10.3847/1538-4357/aaef90)
- Krieger, N., Ott, J., Beuther, H., et al. 2017, ApJ, 850, 77, doi: [10.3847/1538-4357/aa951c](https://doi.org/10.3847/1538-4357/aa951c)
- Kroupa, P. 2001, MNRAS, 322, 231, doi: [10.1046/j.1365-8711.2001.04022.x](https://doi.org/10.1046/j.1365-8711.2001.04022.x)
- Kruijssen, J. M. D., Dale, J. E., & Longmore, S. N. 2015, MNRAS, 447, 1059, doi: [10.1093/mnras/stu2526](https://doi.org/10.1093/mnras/stu2526)

- Lada, C. J., & Lada, E. A. 2003, *ARA&A*, 41, 57, doi: [10.1146/annurev.astro.41.011802.094844](https://doi.org/10.1146/annurev.astro.41.011802.094844)
- Madau, P., & Dickinson, M. 2014, *ARA&A*, 52, 415, doi: [10.1146/annurev-astro-081811-125615](https://doi.org/10.1146/annurev-astro-081811-125615)
- McMullin, J. P., Waters, B., Schiebel, D., Young, W., & Golap, K. 2007, in *Astronomical Society of the Pacific Conference Series*, Vol. 376, *Astronomical Data Analysis Software and Systems XVI*, ed. R. A. Shaw, F. Hill, & D. J. Bell, 127
- Meng, F., Sánchez-Monge, Á., Schilke, P., et al. 2022, *A&A*, 666, A31, doi: [10.1051/0004-6361/202243674](https://doi.org/10.1051/0004-6361/202243674)
- Mills, E. A. C., Ginsburg, A., Clements, A. R., et al. 2018, *ApJL*, 869, L14, doi: [10.3847/2041-8213/aaf237](https://doi.org/10.3847/2041-8213/aaf237)
- Myers, P. C., Hatchfield, H. P., & Battersby, C. 2022, *ApJ*, 929, 34, doi: [10.3847/1538-4357/ac5906](https://doi.org/10.3847/1538-4357/ac5906)
- Ossenkopf, V., & Henning, T. 1994, *A&A*, 291, 943
- Otter, J., Ginsburg, A., Ballering, N. P., et al. 2021, *ApJ*, 923, 221, doi: [10.3847/1538-4357/ac29c2](https://doi.org/10.3847/1538-4357/ac29c2)
- Robitaille, T. P., Whitney, B. A., Indebetouw, R., Wood, K., & Denzmore, P. 2006, *ApJS*, 167, 256, doi: [10.1086/508424](https://doi.org/10.1086/508424)
- Rosolowsky, E. W., Pineda, J. E., Kauffmann, J., & Goodman, A. A. 2008, *ApJ*, 679, 1338, doi: [10.1086/587685](https://doi.org/10.1086/587685)
- Sánchez-Monge, Á., Schilke, P., Schmiedeke, A., et al. 2017, *A&A*, 604, A6, doi: [10.1051/0004-6361/201730426](https://doi.org/10.1051/0004-6361/201730426)
- Schmiedeke, A., Schilke, P., Möller, T., et al. 2016, *A&A*, 588, A143, doi: [10.1051/0004-6361/201527311](https://doi.org/10.1051/0004-6361/201527311)
- Schwörer, A., Sánchez-Monge, Á., Schilke, P., et al. 2019, *A&A*, 628, A6, doi: [10.1051/0004-6361/201935200](https://doi.org/10.1051/0004-6361/201935200)
- Tobin, J. J., Sheehan, P. D., Megeath, S. T., et al. 2020, *ApJ*, 890, 130, doi: [10.3847/1538-4357/ab6f64](https://doi.org/10.3847/1538-4357/ab6f64)
- Williams, J. P., & Cieza, L. A. 2011, *ARA&A*, 49, 67, doi: [10.1146/annurev-astro-081710-102548](https://doi.org/10.1146/annurev-astro-081710-102548)

APPENDIX

A. CLEANING AND SELF-CALIBRATION TESTING

Sgr B2 region is one of the most complex regions that ALMA can observe. Pointing Band 3 beam at one of the two largest cores N or M places the other of the two just on the edge of the beam significantly contributing to the artifacts in the image. We have rigorously tested different cleaning approaches with special focus on masking and choosing the right threshold.

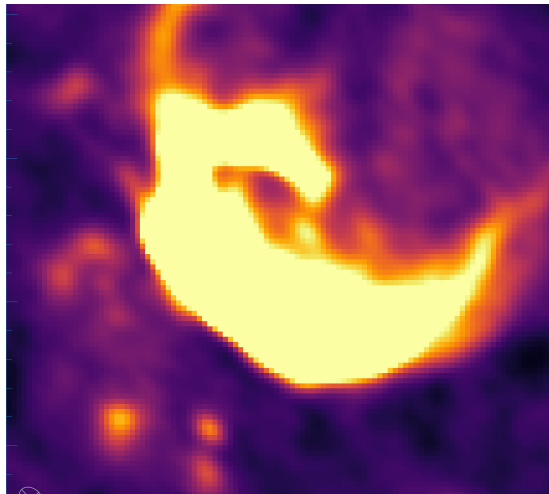
outline: *masks * broad with polygons * strict with polygons * strict with sigmas

During our testing on the best cleaning approach for these data, we determined that using a broader cleaning mask that might include some artifacts reduces the noise in the image more than using more constricting mask. However, using a tighter mask for the first several cleaning iterations and then switching to a broad mask produces just a few percent lower noise compared to using a broader mask throughout the whole process. We also found that decreasing the cleaning threshold decreases the overall image noise even if the model begins to include artifact features.

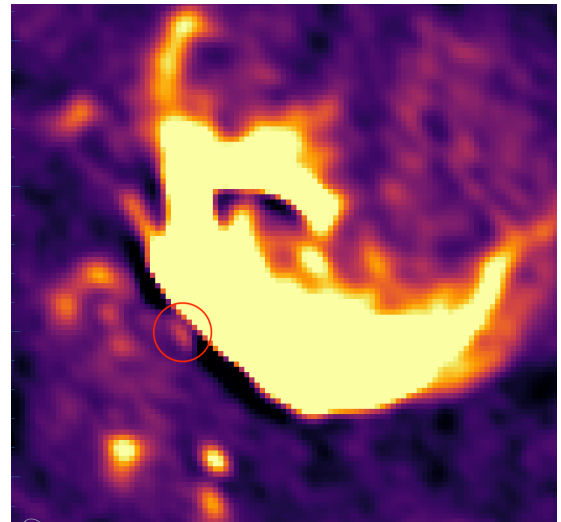
*thresholds for NB6 * diverging until amplitude+phase calibration

A.1. *Evaluation using unsharp masking*

(A paragraph explaining an attempt to evaluate the results of the self-calibration. A note on new detection using this method.)



(a) Final calibrated image of Sgr B2 S H II region and surrounding cores.



(b) The same regions with unsharp mask applied. A new source is now visible very close to the H II region, circled in red. This source blends with the H II region in the original region and cannot be picked up by the source extraction algorithms. Thus, this source is not included in our catalog

Figure 16. Unsharp masking revealing a source very close to a bright H II region.

B. SELF-CALIBRATION: PROGRESS

(Screenshots of different regions at different calibration stages. A few sentences summarizing the results).

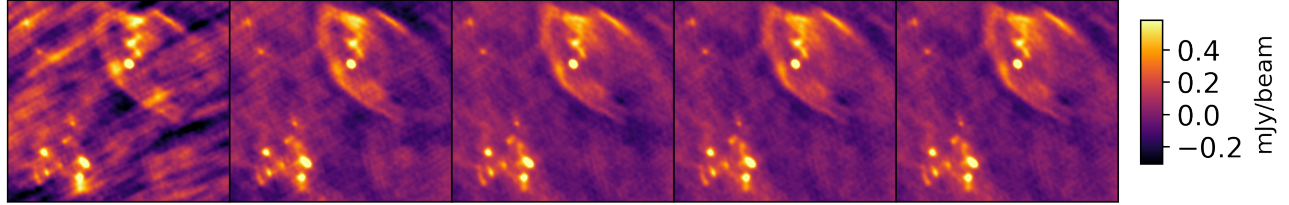


Figure 17. The calibration progress of the highly fragmented source from Sgr B2 M. Sgr B2 Y HII region is visible on the top right. The larger version of this region is shown in figure 3. The iterations from left to right are: uncalibrated, phase, `solint = inf`; phase, `solint = int`; phase and amplitude, `solint = inf`; phase and amplitude, `solint = int`.

C. SOURCE CATALOG

D. RADIAL CORE DISTRIBUTION

We show the core volume number density distribution as a function of distance from the center of each of the two main clusters in Figure 18. The distributions follow a power law with a slope of 2 near the center and increases to 3 at the very edges. This distribution calculation does not take into account the radial decrease in sensitivity of our data so the core number density at large distances is underestimated. A sudden increase in the core number density for Sgr B2 M at 7×10^4 AU is caused by a large number of sources in the vicinity of Sgr B2 South.

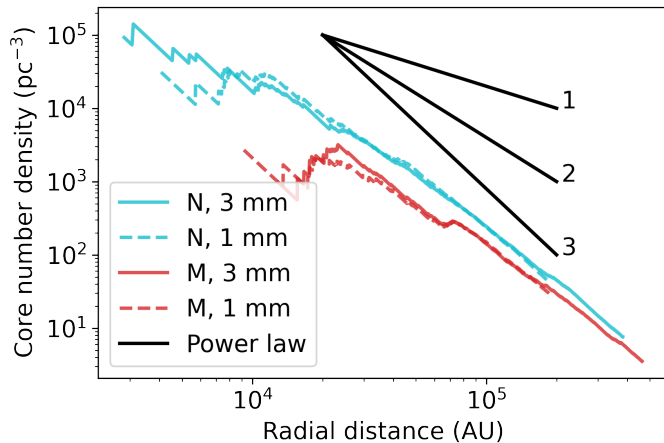


Figure 18. Radial core distribution as a function of number density. Several power law slopes are overplotted. The slope of the core distribution varies from ~ 2 near the center of the clusters to ~ 3 at the edges. The small bump at 7×10^4 AU for Sgr B2 M is due to a large number of cores around Sgr B2 South.

Table 3. First 25 entries of the Sgr B2 N core catalog at 3 mm.

ID	$S_{\nu,flux}$ mJy	$S_{\nu,peak}$ mJy beam $^{-1}$	FWHM $_{maj}$ "	FWHM $_{min}$ "	RA (ICRS)	Dec (ICRS)	Score	G18	T_B K	α	α_{err}	Mass M_{\odot}
1	0.71	0.43	0.115	0.071	17:47:19.884	-28:22:20.316	2	9.0	2.427	0.2364	10.538	
2	1.97	1.48	0.092	0.082	17:47:19.9464	-28:22:19.992	2	30.0	2.125	0.0879	29.267	
3	1.23	1.14	0.076	0.061	17:47:19.9368	-28:22:19.812	2	23.0	2.461	0.0874	18.185	
4	7.2	3.39	0.176	0.059	17:47:19.908	-28:22:19.452	1	68.0	2.023	0.0419	106.871	
6	1.2	1.11	0.098	0.054	17:47:19.9272	-28:22:19.272	2	22.0	2.369	0.0962	17.829	
8	0.67	0.47	0.105	0.072	17:47:19.9632	-28:22:18.84	2	9.0	2.158	0.2719	9.937	
9	0.97	0.71	0.093	0.064	17:47:19.9032	-28:22:18.804	1	14.0	2.239	0.1683	14.432	
11	2.45	1.66	0.115	0.078	17:47:19.9512	-28:22:18.624	2	33.0	1.257	0.1656	36.309	
12	0.37	0.38	0.078	0.06	17:47:20.04	-28:22:18.624	2	8.0	2.813	0.2023	5.434	
16	7.62	2.23	0.163	0.132	17:47:19.8072	-28:22:18.264	1	45.0	2.366	0.0481	113.009	
18	2.33	1.94	0.091	0.052	17:47:19.836	-28:22:18.3	2	39.0	1.781	0.0898	34.603	
20	1.59	1.42	0.095	0.051	17:47:19.9416	-28:22:18.012	1	29.0	1.455	0.1631	23.601	
22	2.96	1.83	0.105	0.067	17:47:19.8408	-28:22:18.012	2	37.0	2.277	0.0629	43.832	
26	0.5	1.33	0.042	0.033	17:47:19.8456	-28:22:17.904	2	27.0	2.034	0.106	7.459	
27	4.61	1.54	0.271	0.063	17:47:19.9416	-28:22:17.724	1	31.0	2.136	0.0836	68.373	
29	0.86	0.77	0.091	0.053	17:47:19.9056	-28:22:17.76	1	15.0	2.516	0.1243	12.828	
31	1.27	3.0	0.062	0.025	17:47:19.98	-28:22:17.58	1	61.0	2.03	0.0469	18.789	
32	7.58	4.69	0.105	0.071	17:47:19.9872	-28:22:17.436	1	95.0	1.867	0.0345	112.496	
33	0.89	1.54	0.06	0.036	17:47:19.8744	-28:22:17.472	2	31.0	2.501	0.0625	13.178	
34	2.72	1.22	0.141	0.093	17:47:19.8408	-28:22:17.436	2	25.0	2.728	0.0668	40.306	
35	3.89	1.93	0.136	0.088	17:47:19.9392	-28:22:17.328	2	39.0	1.839	0.0857	57.75	
37	0.07	0.18	0.046	0.031	17:47:19.8744	-28:22:22.152	2	4.0	3.154	0.3422	1.005	
39	0.09	0.19	0.054	0.037	17:47:19.92	-28:22:21.432	2	4.0	3.418	0.2857	1.372	
40	0.56	0.28	0.115	0.078	17:47:20.0136	-28:22:21.252	1	6.0	2.657	0.3074	8.332	
63	0.1	0.17	0.067	0.033	17:47:19.7568	-28:22:19.848	1	4.0	3.882	0.2521	1.421	

E. FRAGMENTATION VS FLUX

We find that any source from G18's catalog, at 5000 AU resolution, with flux above 20 mJy ended up being fragmented at 500 AU resolution. It is not possible to place meaningful lower limits on the fragmentation function at low flux: the sources are more likely to be close to the sensitivity limit of the higher-resolution data.

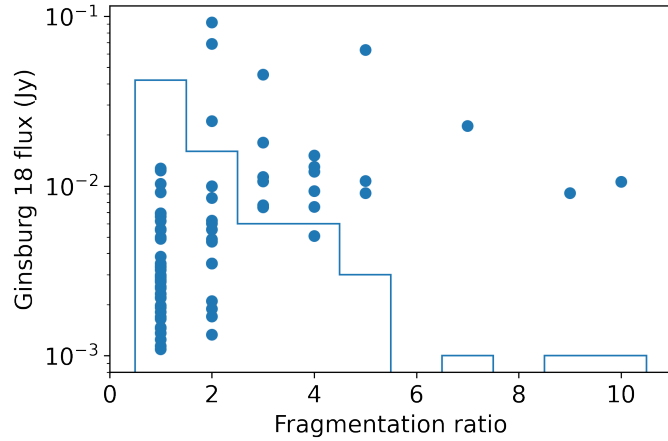


Figure 19. The number of cataloged cores within $1.5 \times$ G18's beam FWHM centered on the G18's detections plotted against G18's flux. The histogram is overplotted over the scatter plot.